PCCP

PAPER

View Article Online
View Journal | View Issue

Cite this: *Phys. Chem. Chem. Phys.*, 2026, **28**, 3963

Magnetism of nanostructured hematite: from cultural heritage to fundamental properties

Sawssen Slimani,*[ab] Alberto Martinelli,[c] Alexander Omelyanchik,[a] Maryam Abdolrahimi,[ab] Elena Castagnotto,[ad] Pierfrancesco Maltoni,[ab] Sara Laureti,[b] Gianni Barucca,[e] Nader Yaacoub,[f] Federico Locardi,[a] Arooj Ramzan,[a] Laura Gaggero,[d] Maurizio Ferretti[a] and Davide Peddis[ab]

Received 14th October 2025,
Accepted 5th January 2026

DOI: 10.1039/d5cp03945b

rsc.li/pccp

This study presents a comprehensive magnetic and morpho-structural investigation of α-Fe_2O_3 nanostructures from two distinct origins: natural (geologically extracted) and synthesized (*i.e.*, laboratory-synthesized by an auto-combustion sol–gel method and commercially purchased hematite). All samples underwent thermal treatments, designed to reproduce color changes typical of hematite pigments in archaeological contexts. Through a combination of DC magnetization measurements and Mössbauer spectroscopy, we demonstrated the possibility of differentiating the origin of hematite nanostructures based on their magnetic behavior. Interestingly, low-temperature NPD analysis revealed that the intensity of the magnetic peak (003) was partially suppressed but not completely extinguished as expected for a perfect antiferromagnetic alignment, which suggests a possible coexistence of weakly ferromagnetic and antiferromagnetic phases in distinct domains below the Morin transition.

1. Introduction

Iron oxide-based nanostructures such as hematite (α-Fe_2O_3), maghemite (γ-Fe_2O_3), and magnetite (Fe_3O_4) have garnered increasing attention due to their rich physicochemical properties and wide-ranging applications.[1–3] These compounds exhibit distinct characteristics in terms of crystal structure, electronic configuration, and magnetic behavior, making them attractive for use in several applications.[4–6] Hematite, in particular, stands out as one of the most studied iron oxides due to its abundance, environmental compatibility and thermal stability.[7,8] Numerous studies have explored hematite as a promising material in fields such as lithium-ion batteries,[9] photocatalysis,[10] gas sensing,[11] water splitting,[12] and biomedical applications.[6] In addition to this already rich plethora of applications, nanostructured hematite exhibits new exciting physical properties,[13–16] enabling advanced applications in catalysis,[17] energy storage and conversion,[6] environmental remediation, and spintronic or magnetic devices. On the other hand, the significant abundance and versatility of natural hematite make it a readily available source of iron oxide. This accessibility is particularly beneficial in fields such as geology, mineralogy, and environmental sciences, where hematite is often studied to understand geological processes and Earth's history; moreover, understanding the behavior of natural hematite can promote sustainable practices.[18,19] The intrinsic properties that make hematite valuable also explain its historical and cultural importance as a pigment since prehistory.[7,20–22] Its distinctive red to reddish-brown color made it a favored material for prehistoric pigments,[23] commonly found in cave paintings,[24] burial sites, and ritualistic objects.[25]

The significance of hematite in several areas of application arises from the intimate interplay between its crystal structure, electronic configuration, and magnetic behavior. These fundamental features not only govern its optical properties but also determine its functional performance in terms of magnetic ordering, charge transport, and electrochemical reactivity. It crystallizes in a trigonal system (space group type $R\bar{3}c$) with a corundum-type structure. Within this structure, iron ions (Fe^{3+}) are octahedrally coordinated by oxygen ions, forming a closely packed arrangement. This octahedral coordination leads to a strong covalent character of the iron–oxygen bonds, contributing to hematite's remarkable thermal, chemical and environmental stability, a key reason it has

---

[a] *Department of Chemistry and Industrial Chemistry & INSTM RU, University of Genoa, Via Dodecaneso 31, Genoa, I-16146, Italy. E-mail: Sawssen.Slimani@edu.unige.it*
[b] *Istituto di Struttura Della Materia (ISM) – CNR, nM2-Lab, Area Della Ricerca di Roma 1, Monterotondo Scalo, RM 00015, Italy*
[c] *SPIN-CNR, C.so Perrone 24, Genova I-16152, Italy*
[d] *Department of Earth, Environment and Life Sciences, University of Genoa, Corso Europa 26, I-16132, Italy*
[e] *Department of Science and Engineering of Matter, Environment and Urban Planning, University Politecnica delle Marche, Via Brecce Bianche 12, Ancona I-60131, Italy*
[f] *Institut des Molécules et Matériaux du Mans CNRS UMR-6283, Le Mans Université, Avenue Messiaen, 72085 Le Mans, France*

endured for millennia in rock art and pigments without significant degradation.[26]

Hematite exhibits a complex magnetic behavior that evolves with temperature. At low temperatures, it is antiferromagnetic (AFM), with Fe^{3+} magnetic moments aligned antiparallel, resulting in no net magnetization. When the temperature rises above the Morin transition ($T_M \approx 263$ K),[27] the spins gradually reorient into the basal plane, producing a weak ferromagnetic (WFM) component due to the Dzyaloshinskii–Moriya interaction.[28,29] In the hexagonal structure, this corresponds to a spin rotation from the [001] axis to the (110) plane, which reflects a change in magnetic anisotropy. Above T_M, the antiparallel arrangement of spins persists, but with a slight canting that explains the onset of WFM ordering. This magnetic landscape provides valuable insights into hematite's thermal history and structural evolution, and it also offers useful tools for archaeometry investigations. For example, magnetic measurements can help distinguish between natural hematite and synthetic analogues.[30] Within this framework, the present study focuses on a comparative investigation of the magnetic properties of natural hematite (NH), laboratory-synthesized hematite (SH), and commercially available hematite (CH). SH and CH samples can be considered as reference materials to benchmark the magnetic behavior of NH samples. In particular, the SH sample is thoroughly characterized, with comprehensive information on its morphological and structural features, magnetic properties, and synthesis processes, including thermal treatments.[31] By contrast, the CH sample may be regarded as the representative of the broader category of commercial materials marketed as "hematite," but often accompanied by limited information concerning their morpho-structural characteristics and the majority of their synthetic procedures, which are often processed on an industrial scale. In particular, the influence of thermal treatment, at 1100 °C for 2 hours in air, on the morpho-structural and magnetic characteristics of different hematite samples was systematically explored. The selected thermal treatment conditions reflect those employed in the preparation of the historical hematite-based pigment Caput Mortuum, traditionally obtained through the calcination of hematite-rich materials at temperatures exceeding 1000 °C.[32] A multi-technique approach combining X-ray powder diffraction (XRPD), transmission electron microscopy (TEM), Mössbauer spectrometry (MS), magnetic measurements (MM), and neutron powder diffraction (NPD) has been used in this study to investigate the morphological, structural, and magnetic differences among the analyzed hematite samples. While conventional techniques, such as XRPD and TEM, offer limited capability in distinguishing between natural and synthetic, or treated forms of hematite in some cases, the integration of MM, MS, and NPD reveals clear and significant differences. The primary objective of this work is to provide a detailed magnetic profile capable of reliably determining the natural or synthetic origin of hematite nanoparticles. This capability is particularly valuable in fields such as archaeology and cultural heritage studies, where identifying the provenance of iron oxide pigments can provide important insights into ancient technologies, traditions and trade networks. Thermal treatments, applied to reproduce color changes typically associated with hematite pigments in archaeological contexts, resulted in a notable change in magnetic behavior depending on the origin of hematite. NPD investigation enables us to better understand the differences in magnetic properties among the samples. Interestingly, low-temperature NPD measurements on SH and NH hematite samples reveal the coexistence of two distinct magnetic phases below T_M, opening new perspectives on the complex magnetic behavior of nanostructured hematite and challenging its conventional understanding.

2. Experimental

2.1. Samples

Natural hematite (NH) was collected from an Italian outcrop (based in Elba Island) in a massive form, and then, it was ground to obtain powders. As reported in our previous work,[32] the EDS mapping of the natural sample consisted of α-Fe_2O_3 accompanied by a silicate–aluminate matrix typical of its geological origin. Synthetic hematite (SH) was obtained by a modified sol–gel auto-combustion method.[33] Briefly, the pH of a solution of $Fe(NO_3)_3 \cdot 9H_2O$ (sigma Aldrich, purity $>98\%$) and citric acid ($C_6H_8O_7$ (Sigma Aldrich, purity$>$ 99.5%), 1 mol L^{-1}) was adjusted to a value of 7 by dropwise adding 30% of ammonia solution. Afterwards, it was dried for 2 hours at 150 °C. Once the gel was obtained, the temperature increased up to 300 °C, leading to a fast combustion reaction. The obtained powder was gently ground in a mortar and then thermally treated at 500 °C in ambient atmosphere to remove the residual organic constituents and to obtain the desired product.

For comparison purposes, a commercially available synthetic hematite sample (CH) Ferroxide® Red 212P, supplied by Rockwood Pigments, was included in this study. CH is a precipitated red iron oxide with an α-Fe_2O_3 content exceeding 97%. This sample, manufactured under strict process and quality control, is widely used in applications, making it a good benchmark for comparison with natural hematite (NH) and synthesized hematite (SH).

Finally, to investigate the effect of thermal treatment, NH, CH and SH samples were subjected to a thermal-oxidative process in a muffle at 1100 °C for 2 hours in air. The obtained samples were labelled as ANH, ACH and ASH, respectively. Samples' labels and their descriptions are summarized in Table 1.

2.2. Characterization and data treatment

Phase identification was carried out by X-ray powder diffraction (XRPD) using an Empyrean X-ray diffractometer (Malvern Panalytical, UK), equipped with a 1.8 kW Cu-K_α ceramic X-ray tube and a PIXcel3D 2 × 2 area detector, operating at 45 kV and 40 mA, in the 2θ range of 5–90°, with a scanning step of 0.02°. Structural refinements were carried out according to the Rietveld method, using the program FullProf. To gain information

Table 1 Summary of samples' codes and their descriptions and phase purity

Sample codes	Reference samples	Main phase	Impurity
NH	Natural hematite	α-Fe_2O_3	Si and Al
ANH	Annealed natural hematite	α-Fe_2O_3 and γ-Fe_2O_3	Impurities inherited from the parent sample
SH	Synthetic hematite	α-Fe_2O_3	No impurities detected
ASH	Annealed synthetic hematite	α-Fe_2O_3	No impurities detected
CH	Commercially purchased hematite	α-Fe_2O_3	No impurities detected
ACH	Annealed and commercially purchased hematite	α-Fe_2O_3	No impurities detected

about the microstructural properties (size and/or strain), a file describing the instrumental resolution function and a Thompson-Cox-Hastings pseudo-Voigt convoluted with axial divergence asymmetry function was used during calculations. Neutron powder diffraction (NPD) data were collected between 1.5 K and 300 K at the DMC beamline of the Paul Scherrer Institute (PSI) using two different wavelengths, $\lambda = 1.4940$ Å and 2.4500 Å, for high intensity (HI) and medium resolution (MR) data, respectively.

The morphology of the samples was investigated by transmission electron microscopy (TEM) using a Philips CM200 microscope operating at 200 kV and equipped with a LaB_6 filament. TEM samples were prepared by dropping a suspension of powder, dispersed in ethanol, on a commercial TEM grid covered with a carbon thin film and maintained in air until complete evaporation of ethanol. Mössbauer spectra were recorded in transmission geometry using the ^{57}Co/Rh γ-ray source mounted on an electromagnetic driving unit submitted to a triangular velocity form. Experiments were carried out at 77 K and 300 K. The fitting procedure was performed using home-made unpublished MOSFIT software involving magnetic sextets and quadrupolar components with Lorentzian lines.

DC magnetization measurements were performed using a superconducting quantum interference device magnetometer (SQUID, Quantum Design). To prevent any movement of the powders during the measurements, epoxy resin glue was used, and all the obtained magnetic data were normalized by the real mass of the measured sample. For the sample with a clear trend to saturation at high field, the saturation magnetization (M_S) was determined by fitting the curves at high field using the Law of Approach to Saturation (LAS).[34] However, for the samples where the antiferromagnetic behavior is dominating, the spontaneous magnetization was determined by an extrapolation to zero of the linear part of magnetization at high field.[35] Magnetization as a function of temperature was measured according to zero-field-cooling (ZFC) and field-cooling (FC) protocols with an applied field of 10 mT. Briefly, the sample was cooled down from 300 K to 5 K at zero field, then the magnetic field was applied and M_{ZFC} was collected during warming up the sample up to 300 K. The same applied field was maintained, and the sample was cooled down to 5 K and M_{FC} was collected during cooling. To ensure optimal thermal homogeneity and stability, the powdered sample was loaded into a low-mass, non-magnetic sample holder, which was securely coupled to the instrument's high-stability helium-gas exchange thermostat. This configuration ensures highly uniform temperature control throughout the entire sample space, with the sample temperature stabilizing within ±0.2 K of the target setpoint. The resulting ZFC/FC curves, as shown in Fig. 4, are smooth and fully reproducible across multiple measurement cycles, thereby validating the reliability and stability of the temperature conditions during the measurements.

3. Results and discussion

X-ray powder diffraction analysis (Fig. S1 in the SI) reveals that all samples (before and after thermal treatment) constitute hematite crystallizing in the trigonal $R\bar{3}c$ space group type. Weak reflections ascribable to secondary phases can be detected only in both NH and ANH natural samples. Rietveld refinement is shown only for the ASH sample (Fig. 1a) as a representative example. The corresponding average crystallite sizes of all samples are reported in Fig. 1b. A comparison between the untreated samples (NH, CH and SH) and their thermally treated counterparts (ANH, ACH and ASH) clearly highlights the effect of annealing on crystallite growth. The mean crystallite size, extracted from Rietveld refinement, increases markedly after thermal treatment in all three systems. This growth is particularly pronounced for the ANH sample, which exhibits the largest crystallite size after annealing (600 nm), suggesting a more effective coarsening process associated with a reduction in grain-boundary density and enhanced structural reorganization, compared to the untreated samples.

Bright-field TEM observations and selected area electron diffraction (SAED) measurements were carried out for all samples (Fig. 2), enabling analysis of particle morphology, size distribution, and crystallinity. The NH sample exhibits considerable variability in both particle shape and size, ranging from 10 to 500 nm (see the NH inset showing a small particle). In contrast, the SH and CH samples display more uniform characteristics. Specifically, particles in the SH sample appear as irregular platelets, 50–300 nm in size, often forming porous agglomerates (the inset of Fig. 2b). CH particles, on the other hand, are predominantly rhomboidal, with well-defined edges and sizes ranging from 20 to 200 nm. SAED patterns confirm the good crystallinity of all samples, with diffraction spots attributable to the hematite phase (the inset of Fig. 2c as an example). In fair agreement with XRPD results, TEM images of the annealed samples reveal an overall increase in average particle size (compare marker values), further evidenced by the darker contrast of the particles in TEM images, indicating reduced electron beam transmission due to increased thickness.

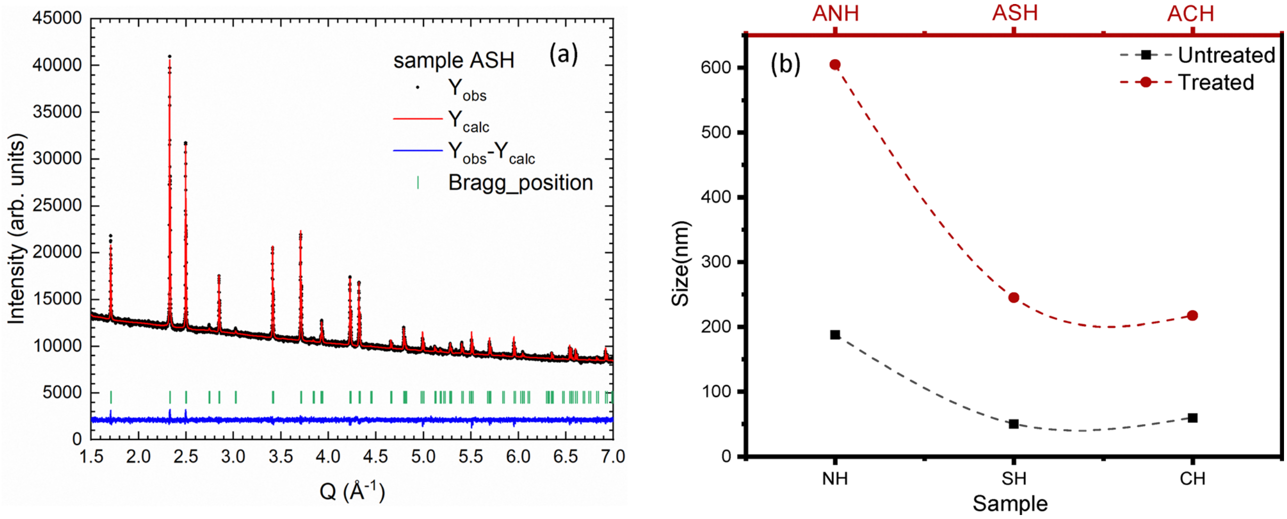

Fig. 1 (a) Rietveld refinement plot for the annealed synthetic hematite (ASH) sample, selected as the representative. (b) Comparison of the mean crystallite size for untreated samples (NH, SH, and CH: black full square symbols) and thermally treated samples (ANH, ASH, and ACH: red full circles). Values were extracted from Rietveld refinement.

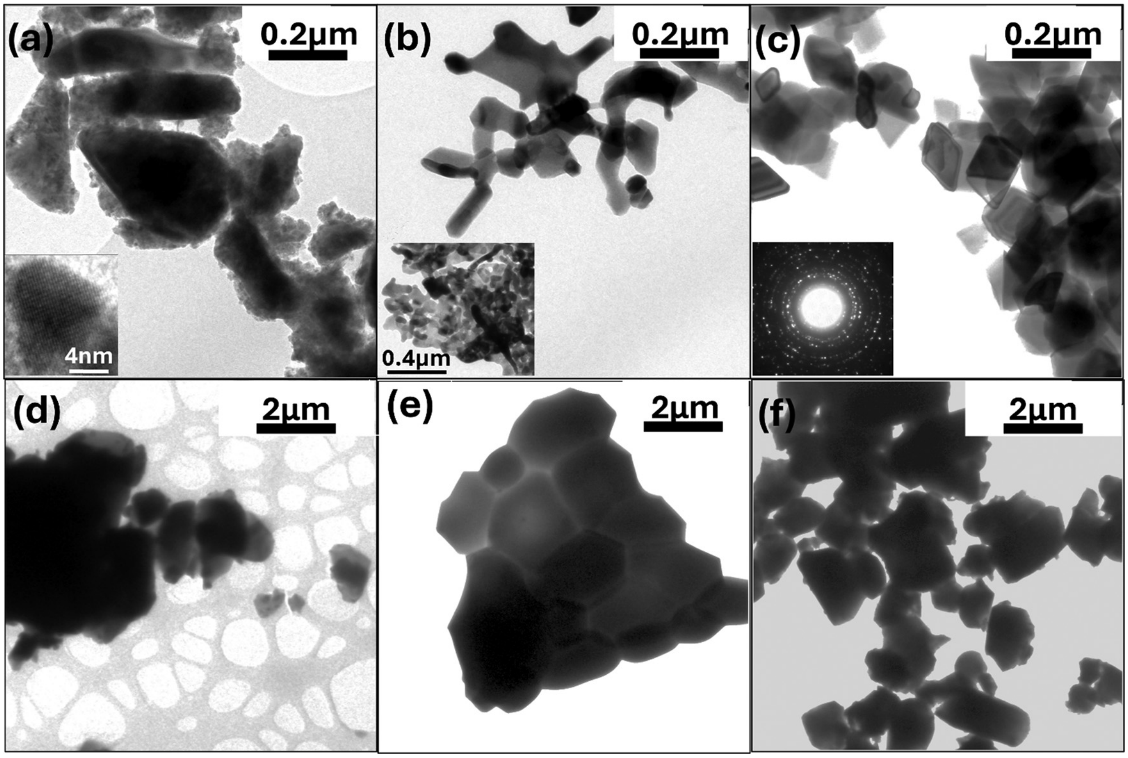

Fig. 2 Bright-field TEM images of untreated samples, (a) NH, (b) SH, and (c) CH, and thermally treated samples, (d) ANH, (e) ASH, and (f) ACH. Inset (a): high-resolution TEM image of a small NH nanoparticle, showing visible hematite atomic planes. Inset (b): large view of a typical SH agglomerate. Inset (c): representative SAED pattern corresponding to the hematite phase in a polycrystalline form.

Interestingly, grain growth in the ASH sample resulted in the formation of particles with a notably regular polygonal shape.

3.1. Hyperfine structures

To obtain information about the hyperfine structure of the samples, Mössbauer spectra were recorded in zero magnetic field below (77 K, Fig. 2) and above (300 K, Fig. S2, in supplementary materials) the T_M. Spectra at 300 K (Fig. S2) show similar results for SH and CH samples, consistent with WFM hematite above the T_M[36–38] whereas the NH spectrum can be fitted with two sextets showing positive and negative quadrupole shifts (2ε), indicating a different hyperfine environment.

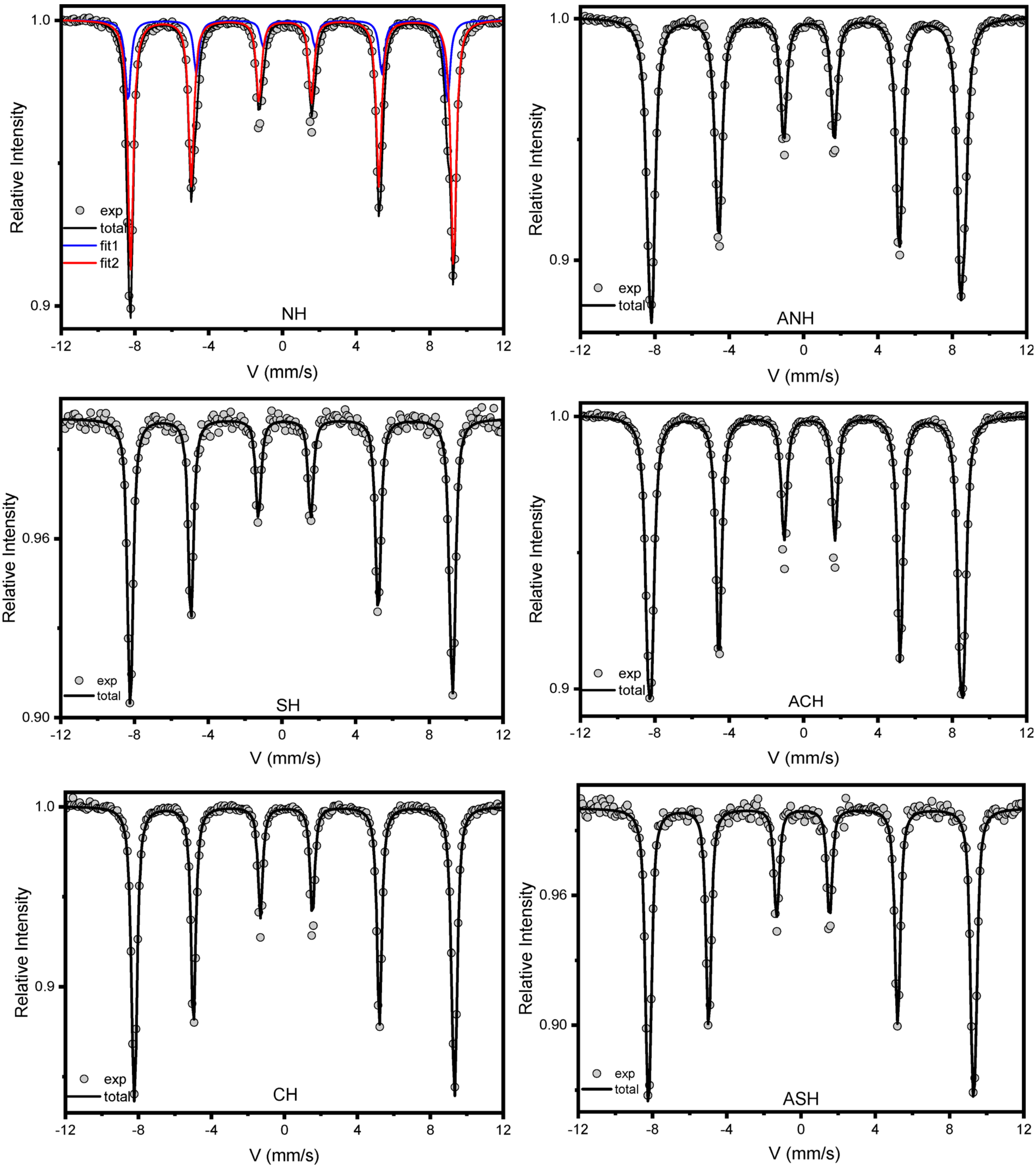

Fig. 3 Mössbauer spectra in zero magnetic field, recorded at 77 K before annealing (NH, SH, and CH) and after annealing (ANH, ASH, and ACH).

In particular, the negative value of 2ε is related to the WFM hematite, and the positive value is relative to a secondary phase such as maghemite (γ-Fe_2O_3) or magnetite (Fe_3O_4).[39,40] Mössbauer spectra below the T_M (77K; Fig. 3 and the fit parameters are reported in Table 1), allow us to better understand the change in magnetic order on the samples NH, SH and CH below the Morin transition.[41] For the NH sample, the values of 2ε were distinctly changed from −0.164 mm s^{-1} to 0.377 mm s^{-1}, from 0.35 mm s^{-1} to −0.08 mm s^{-1} and from 300 K to 77 K, respectively, confirming the coexistence of two distinct magnetic phases. For SH and CH samples, the hyperfine parameters correspond to the stoichiometric hematite with a collinear AFM order below the T_M. Mössbauer spectra at 77 K for all the annealed samples at 1100 °C were fitted with only one component. The fitted lines agree with those of the hematite structure, and the obtained parameters (Table 1) match those of stoichiometric hematite.[42] From this analysis, it becomes evident that MS, even when performed at 300 K, is capable of clearly distinguishing between natural hematite samples and lab synthetic/commercial counterparts. This highlights the sensitivity of MS to subtle differences in hyperfine parameters, which are strongly connected with the sample's origin and synthesis route.

3.2. Magnetic properties

The temperature dependence of magnetization of all the untreated and treated samples was investigated using zero-field-cooled (M_{ZFC}) and field-cooled (M_{FC}) protocols (Fig. 4). The CH sample shows the characteristic Morin transition[43,44] at ∼230 K, with a pronounced increase in magnetization at T_M, followed by a relatively constant magnetization of up to 300 K(Fig. 4a). This behavior indicates the coexistence of WF and AFM phases, which is a typical feature of hematite.[16] The NH and SH samples, however, show no evidence of the Morin transition, even though, as discussed later, NPD measurements provide clear evidence of the transition. The inability to observe T_M in magnetization measurements can be ascribed to several factors, such as the reduced particle size, surface anisotropy or the presence of a secondary phase.[16,45,46] Indeed, the NH and SH samples exhibit higher magnetization at low temperatures, which may mask the observation of the Morin transition.

After thermal treatment at 1100 °C, all the samples show T_M (Fig. 4b and Table 3) as an indication of the dominance of the hematite phase. ASH and ACH samples show T_M values close to the theoretical one of 263 K, while the ANH sample shows lower temperatures, suggesting the presence of chemical impurities or still other magnetic phases, also detectable by XRD.[47,48]

Field dependence of magnetization (Fig. 5) was also performed for all the samples below (5 K) and above the Morin temperature (300 K). To interpret these measurements, it is important to underline that below T_M, hematite exhibits collinear antiferromagnetic ordering with Fe^{3+} spins aligned along the *c*-axis, governed by strong uniaxial magnetocrystalline anisotropy.[49] Above T_M, however, the magnetocrystalline anisotropy decreases while the Dzyaloshinskii–Moriya interaction becomes dominant, inducing spin canting and creating a weak ferromagnetic state. This leads to effective anisotropy due to spin canting, despite the reduction in intrinsic magnetocrystalline anisotropy. These competing interactions introduce higher energy barriers for magnetization reversal, ultimately leading to significant enhancement of coercivity at room temperature.[35] At 5 K, both treated (Fig. 5a) and untreated samples (Fig. 5c) show low coercivity, indicating lower anisotropy. Additionally, the NH sample exhibits a distinct ferromagnetic-like hysteresis loop with a low M_s (Table 2), confirming the presence of other magnetic phases in the natural matrix. SH and CH samples display at 5 K an antiferromagnetic response at high fields, superimposed on a weak ferromagnetic trend at low fields, with the latter effect being most pronounced in SH. This behavior can be attributed to the presence of uncompensated spins or, less likely, to the presence of a small percentage of ferro(i)magnetic phases.[32,33] These effects are also closely connected to the origin and preparation route of the samples. The synthetic hematite (SH) sample, produced by rapid combustion, consists of irregular platelet-like particles forming porous agglomerates. Such a morphology implies a high surface-to-volume ratio and a large density of surface and interfacial spins, which can enhance spin disorder and surface canting. Conversely, the commercial hematite (CH) sample is characterized by predominantly well-defined rhomboidal crystals with sizes in the 20–200 nm range, indicative of a higher degree of structural regularity and reduced surface disorder. In contrast, natural hematite inherently presents complex and spatially inhomogeneous distributions of impurities, defects, and internal strain, which cannot be independently tuned. These morphological and structural differences are therefore expected to directly affect the coercive field and the temperature-dependent magnetic behavior observed in the ZFC/FC measurements.[50]

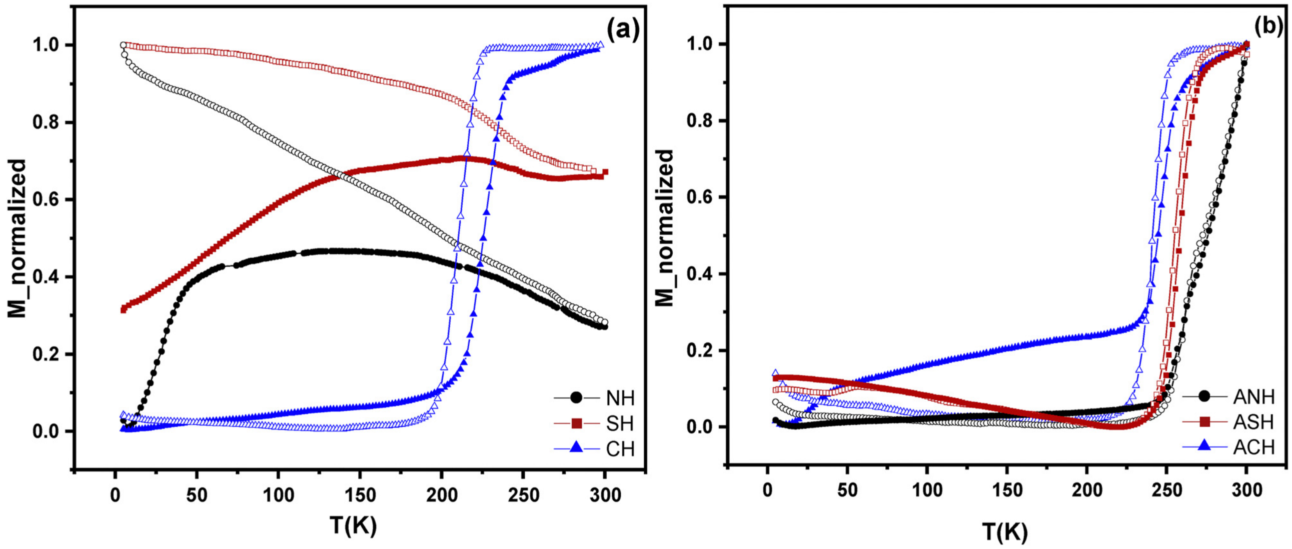

Fig. 4 (a) Zero-field-cooled (ZFC, filled symbols) and field-cooled (FC, open symbols) curves for untreated samples (NH, CH, and SH). (b) ZFC/FC curves for the corresponding annealed samples (ANH, ACH, and ASH).

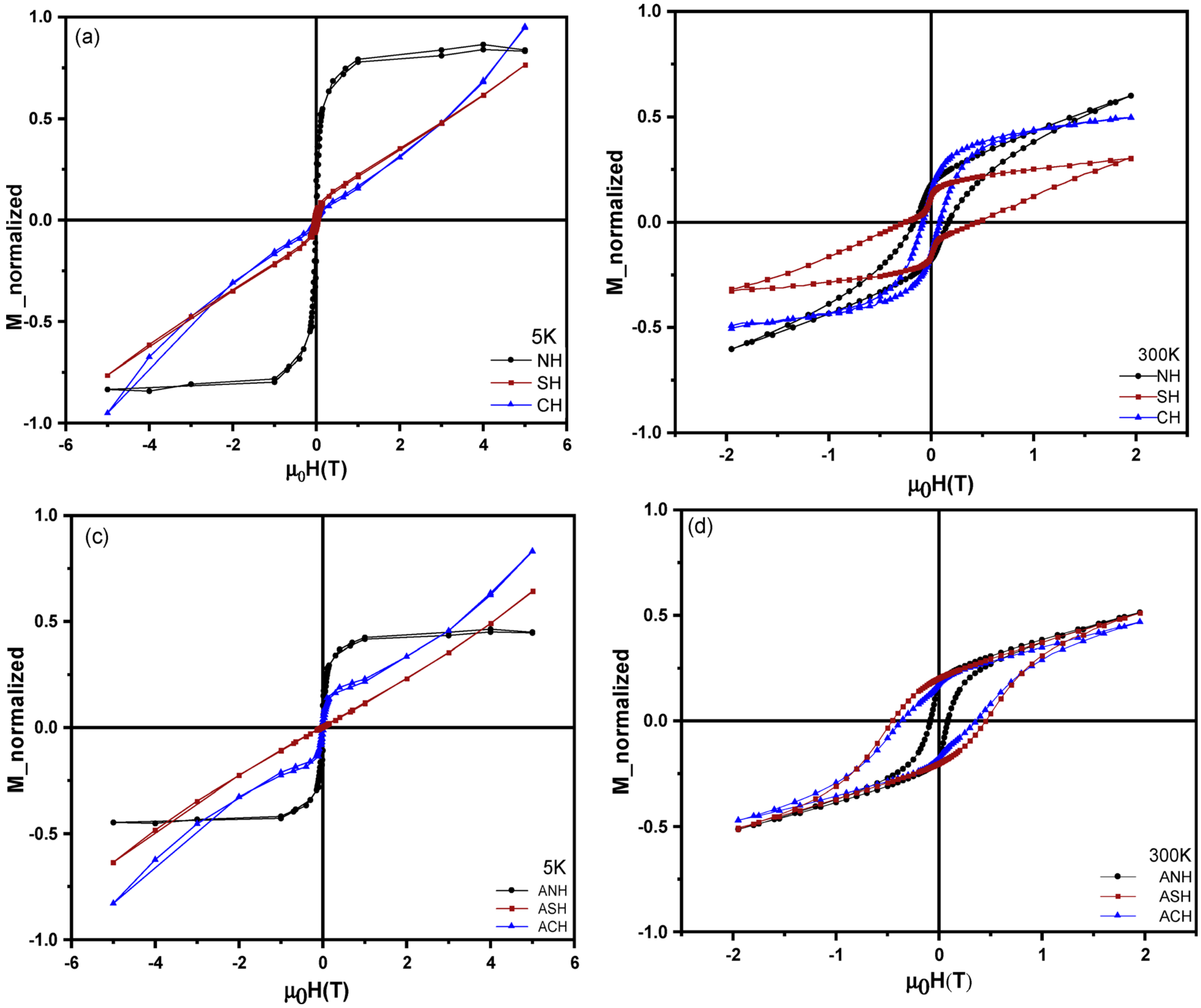

Fig. 5 Field-dependent magnetization curves measured at (a) 5 K and (b) 300 K before thermal treatment (NH, SH, and CH), and at (c) 5 K and (d) 300 K after thermal treatment (ANH, ASH, and ASH).

Table 2 Data extracted from the fit of the Mössbauer spectra at 77 K. Isomer shift (δ), quadrupole shift (2ε), hyperfine magnetic field (B_{hyp}) and relative percentage area of the components. Uncertainty is giving on the last digit

Sample		δ (mm s^{-1})	2ε (mm s^{-1})	B_{hyp} (T)	Area (%)
NH	Fit1	0.49(2)	0.38(2)	53.5(1)	75(2)
	Fit2	0.50(2)	-0.08(2)	54.1(1)	25(2)
ANH		0.50(2)	0.40(2)	54.2(1)	
SH		0.49(2)	0.37(2)	54.0(1)	
ASH		0.49(2)	0.43(2)	54.1(1)	
CH		0.50(2)	0.43(2)	54.2(1)	
ACH		0.49(2)	0.37(2)	54.2(1)	

To quantify the origin of this small contribution, the effective magnetic moment, M_{eff}, (Table 3) is estimated by the extrapolation of high linear portion at high field.[16,51]

At 5 K, the ANH sample still exhibits a ferromagnetic-like behavior, though with a lower M_s compared to the NH sample. This can be attributed to the partial transformation of ferrimagnetic phases (*e.g.* Fe_3O_4 and γ-Fe_2O_3) into an antiferromagnetic phase such as hematite. The ASH samples exhibit nearly pure antiferromagnetic behavior, while the ACH samples show some weak ferromagnetic-like features.

At 300 K, the magnetic properties of all samples undergo significant changes. In both treated and untreated samples, the increase in H_c above T_M arises from the change in magnetic anisotropy, as discussed previously. Notably, the SH sample shows a kink around zero field, suggesting the coexistence of antiferromagnetic and ferrimagnetic phases that are not coupled to each other.[52] At 300 K, the annealed samples show an increase in H_c and M_r (Table 2) compared to their untreated forms, reflecting an increase in magnetic anisotropy, particularly for ASH and ACH. Several studies have demonstrated that nanostructured hematite can exhibit exceptionally high Hc. Pseudocubic α-Fe_2O_3 particles ($\sim$650 nm) have been reported to exhibit $H_c \backsimeq 4$ kOe, even if measured in minor loops, attributed to the internal sub-particle microstructure.[52] Hematite pseudocubic structures exhibit H_c of up to $\sim$5.85 kOe due

Table 3 Morin transition temperature (T_M), saturation magnetization (M_S), and coercive field ($\mu_0 H_C$) at 5 K and 300 K[a]

Sample	T_M (K)	M_s_5 K (Am^2 Kg^{-1})	M_5 K (Am^2 Kg^{-1})	M_300 K (Am^2 Kg^{-1})	$\mu_0 H_c$_5 K (mT)	$\mu_0 H_c$_300 K (mT)
NH	221.5(8.5)[b]	1.01(4)		1.14(2)	12(1)	160(30)
ANH	257(4)	0.45(3)		0.92(1)	12(1)	84(2)
SH	217(11)[b]	—	0.08(4)	0.80(4)	48(4)	280(40)
ASH	259(5)	—	0.05(5)	0.93(2)	—	450(30)
CH	230(3)	—	0.16(3)	0.59(5)	17(4)	82(1)
ACH	246(3)	—	0.04(3)	0.98(4)	22(1)	360(30)

[a] Uncertainty is given on the last digit. [b] Values extracted from neutron diffraction data.

to aggregation-induced pinning mechanisms.[53] More extreme behavior was observed in hematite/SiO$_2$ nanocomposites prepared by a sol–gel route and annealed at 1100 °C: these showed coercivity of up to ~8.5 kOe at 300 K, explained by sub-particle structures and interface effects.[53] While the annealed synthetic (ASH) and commercial (ACH) hematite show an increase in H_c, the annealed natural hematite (ANH) shows a decrease in H_c. This distinct behavior originates from the intrinsic chemical and microstructural constraints of the natural precursor. The phase-pure synthetic (SH) and commercial (CH) hematite undergo a well-defined, uniform crystallite growth during annealing, leading to a pronounced development of magnetocrystalline anisotropy and, consequently, a significant rise in coercivity. In contrast, the natural hematite (NH) sample contains inherent silicate–aluminate impurities, as confirmed by EDS analysis reported in the previous work, and possesses a higher degree of initial structural heterogeneity. Upon annealing, these impurities prevent uniform grain growth and the formation of a homogeneous microstructure. The residual impurity phases and persistent microstructural disorder in ANH thus constrain the full development of magnetocrystalline anisotropy, resulting in a decrease in the Hc compared to ASH and ACH samples.

These findings clearly demonstrate how morphology, thermal treatment, and microstructural features can critically enhance the coercive field of hematite nanostructures.

3.3. The magnetic structure

To better understand the differences in magnetic properties among the various samples, neutron powder diffraction (NPD) patterns were collected between 1.5 K and 300 K for all of them. All NPD patterns exhibit overlapping nuclear and magnetic scattering.

Considering them as the representative of natural and synthetic hematite, the fast-scan high-intensity (HI) data collected during cooling for the NH (Fig. 6a) and SH (Fig. S3) samples are reported. Both samples exhibit magnetic peaks at 1.37, 1.51 and 1.71 Å^{-1} that can be indexed according to a k = (0,0,0) magnetic propagation wavevector.[54,55] The 003 and 101 magnetic reflections at Q = 1.37 Å^{-1} and Q = 1.51 Å^{-1}, respectively, are highly sensitive to the Morin transition. In particular, below the T_M, hematite is in the easy-axis antiferromagnetic state, with spins aligned along the c-axis; hence, the 003 reflection is almost completely suppressed, whereas the intensity of the 101 reflection increases.

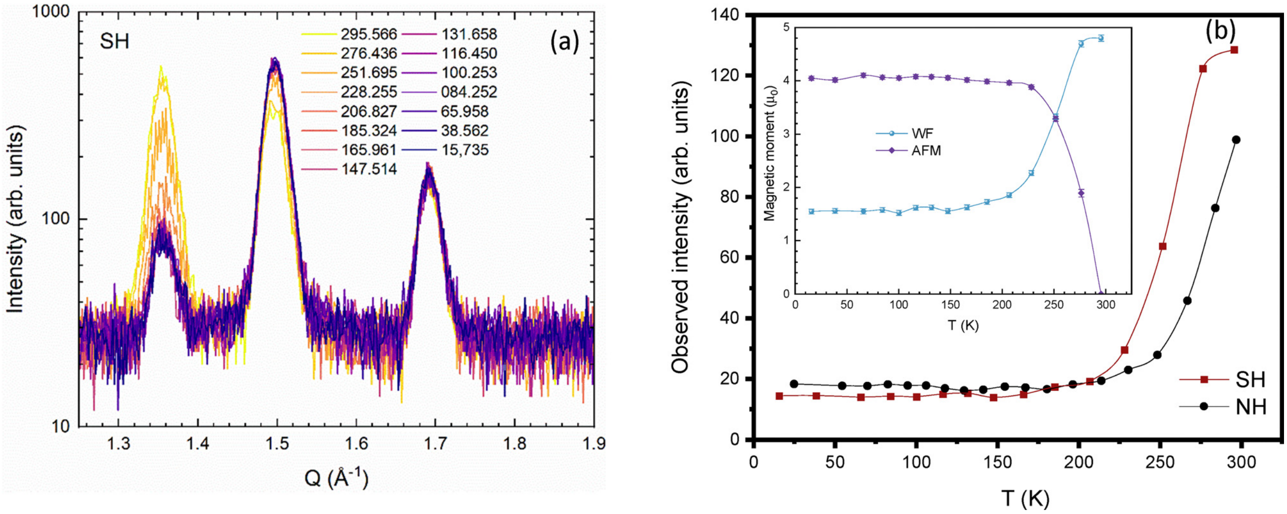

Fig. 6 (a) NPD-MR data for SH samples collected on cooling and evidencing the magnetic transition occurring around 220 K; the intensity scale is plotted using a logarithmic scale to better highlight the small, but sizeable contribution of the magnetic peak 003 at ~1.35 Å^{-1}. (b) Temperature-dependent evolution of the observed peak intensity for SH and NH samples (see also Fig. S3). Both samples show a significant increase of the 003 peak intensity above ~220–250 K, indicating the transition from the antiferromagnetic (AFM) to the weak ferromagnetic (WF) phase, consistent with the Morin transition. The inset shows the magnetic moment evolution of the AFM and WF phases for the SH sample, as obtained from Rietveld refinement (the values are plotted as real magnetic moments, to emphasize the temperature-dependent trend of each phase).

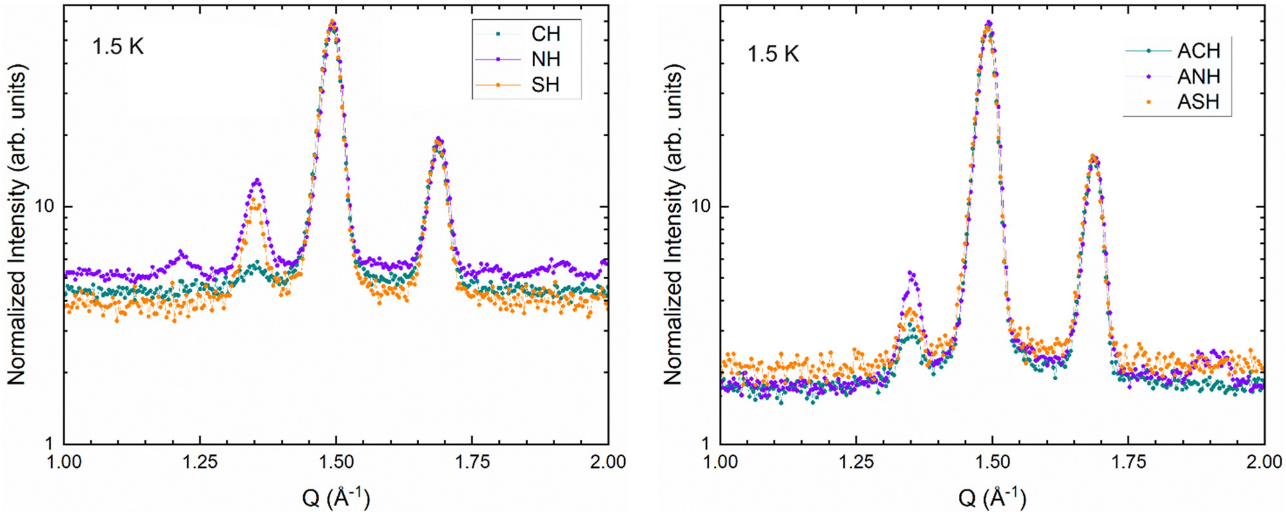

Fig. 7 Superposition of the HI-NPD data collected at 1.5 K showing the contribution of magnetic scattering in the low-Q region of the diffraction pattern; the intensity scale is plotted using a logarithmic scale. A very weak magnetic peak at 1.23 Å^{-1} is observed in the NH sample that cannot be indexed within the hematite structure.

Above T_M, the spins flip into the basal plane, forming the easy-plane weak-ferromagnetic state; as a result, the 003 peak gains intensity, confirming the sole presence of the weak ferromagnetic (WFM) phase at room temperature. In contrast, the 012 reflection at $Q = 1.71$ Å^{-1} is essentially nuclear in origin and remains nearly unaffected, making it a reliable reference. By analyzing the temperature dependence of the 003 magnetic reflection, it can be established that the T_M appears at 221.5(8.5) K and 217(11) K for the NH and SH samples (Fig. 6b main panel), respectively. This finding is particularly interesting, as T_M was not fully observed from the ZFC-FC measurements for the NH and SH samples. Remarkably, the 003 magnetic reflection intensity is not totally suppressed below T_M for SH and NH samples. This feature, which is still debated in the literature,[54,56] could possibly indicate a coexistence of separated domains between the WFM and the AFM phases at low temperatures, or an in-plane component of the AFM phase that produces a slight spin tilting along the *c*-axis. Further extended studies are in progress in order to unveil the exact magnetic ordering. A closer inspection of the NPD data collected at 1.5 K (Fig. 7) shows two additional features. A very weak, faint magnetic peak at 1.23 Å^{-1} is observed in the NH sample; this peak cannot be indexed with the same propagation vector, and its intensity remains constant in the whole inspected temperature range. This is a clear indication that at least one other spurious magnetic phase is present in the NH sample. This peak disappears in the thermally treated samples (ANH), confirming the total transformation to AFM hematite.

4. Conclusions and perspectives

This paper focuses on a comparative investigation carried out on the morphological, structural, and magnetic properties of natural (NH), synthetic (SH), and commercially acquired (CH) hematite samples, before and after thermal treatment at 1100 °C for 2 h, a treatment condition of particular interest for cultural heritage applications. A multi-technique approach was employed, combining XRPD, TEM, MS, magnetometry and NPD. Interestingly, the NH sample displays more complex magnetic features due to the presence of other magnetic phases that have been observed from the $M(H)$ curve. The thermal treatment at 1100 °C significantly enhanced crystallinity, inducing particle growth in all samples; annealed samples show AFM behavior, confirming the dominance of the hematite phase. However, residual WFM behavior in the ANH sample suggests the persistence of secondary magnetic phases related to its geological origin. Notably, this paper demonstrates that despite XRD and TEM measurements alone not allowing to distinguish between synthetic hematite and natural hematite, analysis of magnetic properties and hyperfine structures allows the hematite provenance to be clearly distinguished. These results offer new interesting perspectives in the geological and cultural heritage fields. To further understand the differences in magnetism between the samples, low-temperature NPD suggests the coexistence of two distinct magnetic phases, AFM and WFM, below T_M. These results provide a description of how the synthesis route and thermal annealing affect the structural and magnetic properties of hematite nanostructures. At the same time, they raise more fundamental questions. In particular, our findings suggest a possible coexistence of weakly ferromagnetic and antiferromagnetic phases below the Morin transition. Preliminary indications such as those hinted by low-temperature neutron powder diffraction highlight the critical yet still insufficiently explored roles of internal strain distributions, in shaping the magnetic signatures of hematite, well-established and extensively studied system. Taken together, these observations clearly position this work as a basis for future studies and motivate further investigations of hematite nanostructures using advanced neutron diffraction techniques and local probes such as high-field Mössbauer spectroscopy and, which will be essential for understanding the origin and nature of the observed magnetic behavior.

Conflicts of interest

There are no conflicts to declare.

Data availability

The data supporting this study are available in the main article and the supplementary information (SI). Supplementary information: additional X-ray powder diffraction patterns of all the samples, Mössbauer spectra recorded at 300 K under zero field and NPD-MR data for the NH sample collected on cooling. See DOI: https://doi.org/10.1039/d5cp03945b.

The main manuscript contains morpho-structural and magnetic characterization, namely the XRD pattern with the Rietveld refinement of ASH (as an example) and the mean crystallite size for all the samples, bright-field TEM images, Mössbauer spectra recorded at zero field at 77 K, zero-field-cooled (ZFC) and field-cooled (FC) curves and field-dependent magnetization curves measured at (a) 5 K and (b) 300 K for all the samples from neutron measurements, NPD-MR data for SH samples collected on cooling and HI-NPD data (for SH and CH) collected at 1.5 K have been reported.

Acknowledgements

The authors acknowledge the support from Project code PE0000021, Concession Decree No. 1561 of 11.10.2022 adopted by ''Ministero dell'Universitá e della Ricerca (MUR)'', according to attachment E of Decree No. 1561/2022, Project title ''Network 4 Energy Sustainable Transition-NEST''.

References

1 M. A. Blesa and E. Matijević, Phase transformations of iron oxides, oxohydroxides, and hydrous oxides in aqueous media, *Adv. Colloid Interface Sci.*, 1989, **29**, 173–221, DOI: 10.1016/0001-8686(89)80009-0.
2 G. Muscas, F. Congiu, C. Cannas, V. Mameli, N. Yaacoub, R. S. Hassan, D. Fiorani, S. Slimani and D. Peddis, The Boundary Between Volume and Surface-Driven Magnetic Properties in Spinel Iron Oxide Nanoparticles, *Nanoscale Res. Lett.*, 2022, **17**, 98, DOI: 10.1186/s11671-022-03737-w.
3 A. Shahzad, B. Aslibeiki, S. Slimani, S. Ghosh, M. Vocciante, M. Grotti, A. Comite, D. Peddis and T. Sarkar, Magnetic nanocomposite for lead (II) removal from water, *Sci. Rep.*, 2024, **14**, 17674, DOI: 10.1038/s41598-024-68491-8.
4 I. Khan, A. Khalil, F. Khanday, A. M. Shemsi, A. Qurashi and K. S. Siddiqui, Synthesis, Characterization and Applications of Magnetic Iron Oxide Nanostructures, *Arab. J. Sci. Eng.*, 2018, **43**, 43–61, DOI: 10.1007/s13369-017-2835-1.
5 F. Scarpa and S. Slimani, Galinstan liquid metal as the heat transfer fluid in magnetic refrigeration, *Appl. Therm. Eng.*, 2023, **232**, 120971, DOI: 10.1016/j.applthermaleng.2023.120971.
6 H. Wan, L. Hu, X. Liu, Y. Zhang, G. Chen, N. Zhang and R. Ma, Advanced hematite nanomaterials for newly emerging applications, *Chem. Sci.*, 2023, **14**, 2776–2798, DOI: 10.1039/D3SC00180F.
7 N. Nurdini, M. M. Ilmi, E. Maryanti, P. Setiawan and G. T. M. Kadja Ismunandar, Thermally-induced color transformation of hematite: insight into the prehistoric natural pigment preparation, *Heliyon*, 2022, **8**, e10377, DOI: 10.1016/j.heliyon.2022.e10377.
8 K. J. Vaughn, M. L. Grados, J. W. Eerkens and M. J. Edwards, Hematite mining in the ancient Americas: Mina Primavera, A 2,000 year old Peruvian mine, *JOM*, 2007, **59**, 16–20, DOI: 10.1007/s11837-007-0145-x.
9 H. Watanabe, H. Usui, Y. Domi, K. Uetake, N. Oishi, N. Nitta, H. Kurokawa and H. Sakaguchi, Solid-state lithium batteries composed of hematite and oxide electrolyte, *Mater. Lett.*, 2024, **368**, 136674, DOI: 10.1016/j.matlet.2024.136674.
10 S. Nasejje, E. P. Mukhokosi, M. Diale and D. Velauthapillai, Device architectures for photoelectrochemical water splitting based on hematite: a review, *Discover Mater.*, 2024, **4**, 44, DOI: 10.1007/s43939-024-00112-7.
11 L. F. Da Silva, A. C. Catto, S. Bernardini, T. Fiorido, J. V. N. De Palma, W. Avansi, K. Aguir and M. Bendahan, BTEX gas sensor based on hematite microrhombuses, *Sens. Actuators, B*, 2021, **326**, 128817, DOI: 10.1016/j.snb.2020.128817.
12 S. Stanescu, T. Alun, Y. J. Dappe, D. Ihiawakrim, O. Ersen and D. Stanescu, Enhancement of the Solar Water Splitting Efficiency Mediated by Surface Segregation in Ti-Doped Hematite Nanorods, *ACS Appl. Mater. Interfaces*, 2023, **15**, 26593–26605, DOI: 10.1021/acsami.3c02131.
13 A. R. B. de Castro and R. D. Zysler, A Monte Carlo model of the MCD behavior of hematite colloids, *J. Magn. Magn. Mater.*, 2003, **257**, 51–57, DOI: 10.1016/S0304-8853(02)00985-X.
14 F. Bødker, M. F. Hansen, C. B. Koch, K. Lefmann and S. Mørup, Magnetic properties of hematite nanoparticles, *Phys. Rev. B:Condens. Matter Mater. Phys.*, 2000, **61**, 6826–6838, DOI: 10.1103/PhysRevB.61.6826.
15 A. H. Hill, F. Jiao, P. G. Bruce, A. Harrison, W. Kockelmann and C. Ritter, Neutron Diffraction Study of Mesoporous and Bulk Hematite, α-Fe_2O_3, *Chem. Mater.*, 2008, **20**, 4891–4899, DOI: 10.1021/cm800009s.
16 L. Suber, P. Imperatori, A. Mari, G. Marchegiani, M. V. Mansilla, D. Fiorani, W. R. Plunkett, D. Rinaldi, C. Cannas, G. Ennas and D. Peddis, Thermal hysteresis of Morin transition in hematite particles, *Phys. Chem. Chem. Phys.*, 2010, **12**, 6984–6989, DOI: 10.1039/b925371h.
17 P.-Y. Tang and J. Arbiol, The rise of single-atom catalysts in hematite photoanodes for photoelectrochemical water splitting, *Innovation*, 2025, **6**, 100810, DOI: 10.1016/j.xinn.2025.100810.

18 L. Courtney-Davies, M. Fiorentini, H. Dalstra, S. Hagemann, E. Ramanaidou, M. Danišik, N. J. Evans, K. Rankenburg and B. I. A. McInnes, A billion-year shift in the formation of Earth's largest ore deposits, *Proc. Natl. Acad. Sci. U. S. A.*, 2024, **121**, e2405741121, DOI: 10.1073/pnas.2405741121.

19 A. Jayan, V. Vijayan, S. Sreekantan, S. Arya, P. K. Krishnaprasad, M. Santosh and E. Shaji, Hematite nanomaterial from a tropical freshwater ecosystem: Geological, environmental, and industrial implications, *Sci. Total Environ.*, 2024, **951**, 175611, DOI: 10.1016/j.scitotenv.2024.175611.

20 I. Domingo and A. Chieli, Characterizing the pigments and paints of prehistoric artists, *Archaeol. Anthropol. Sci.*, 2021, **13**, 196, DOI: 10.1007/s12520-021-01397-y.

21 D. E. Rosso, M. Regert and F. d'Errico, First identification of an evolving Middle Stone Age ochre culture at Porc-Epic Cave, Ethiopia, *Sci. Rep.*, 2023, **13**, 13261, DOI: 10.1038/s41598-023-39957-y.

22 D. Kiseleva, E. Shagalov, E. Pankrushina, V. Shirokov, A. Khorkova and D. Danilov, Microanalytical Investigation of Prehistoric Colorants from Uralian Rock Art (Ignatievskaya Cave and Idrisovskaya II and Zmiev Kamen' Pictographs), *Heritage*, 2022, **6**, 67–89, DOI: 10.3390/heritage6010004.

23 E. C. Velliky, M. Porr and N. J. Conard, Ochre and pigment use at Hohle Fels cave: Results of the first systematic review of ochre and ochre-related artefacts from the Upper Palaeolithic in Germany, *PLoS One*, 2018, **13**, e0209874, DOI: 10.1371/journal.pone.0209874.

24 E. Maryanti, M. M. Ilmi, N. Nurdini, P. Setiawan, Y. M. Syah, C. Saiyasombat and G. T. M. Kadja Ismunandar, Hematite as unprecedented black rock art pigment in Jufri Cave, East Kalimantan, Indonesia: the microscopy, spectroscopy, and synchrotron X-ray-based investigation, *Archaeol. Anthropol. Sci.*, 2022, **14**, 122, DOI: 10.1007/s12520-022-01591-6.

25 M. Marinova, Relative Analogies in the Ritual Use of Red Mineral Pigments (Ochre, Hematite) in Neolithic and Eneolithic Burials from Xinjiang and Bulgaria, ed. X. Li, in *Major Archaeological Discoveries Along the Chinese Silk Road*, Springer Nature Singapore, Singapore, 2023, pp. 31–49, DOI: 10.1007/978-981-99-0659-8_4.

26 R. M. Cornell and U. Schwertmann, *The Iron Oxides*, Wiley-VCH Verlag GmbH & Co. KGaA, Weinheim, FRG, 2003, DOI: 10.1002/3527602097.

27 S. Xu, A. H. Habib, S. H. Gee, Y. K. Hong and M. E. McHenry, Spin orientation, structure, morphology, and magnetic properties of hematite nanoparticles, *J. Appl. Phys.*, 2015, **117**, 17A315, DOI: 10.1063/1.4914059.

28 T. Moriya, Anisotropic superexchange interaction and weak ferromagnetism, *Phys. Rev.*, 1960, **120**, 91–98, DOI: 10.1103/PhysRev.120.91.

29 V. Dvořák, A Thermodynamic Theory Of "Weak" Ferromagnetism Of Antiferromagnetics, *Phys. Status Solidi B*, 1971, **46**, 763–772, DOI: 10.1002/pssb.2220460236.

30 M. Tahir, M. Fakhar-e-Alam, M. Atif, G. Mustafa and Z. Ali, Investigation of optical, electrical and magnetic properties of hematite α-Fe2O3 nanoparticles via sol-gel and co-precipitation method, *J. King Saud Univ., Sci.*, 2023, **35**, 102695, DOI: 10.1016/j.jksus.2023.102695.

31 P. Maltoni, G. Varvaro, N. Yaacoub, G. Barucca, J. P. Miranda-Murillo, J. Tirabzonlu, S. Laureti, D. Fiorani, R. Mathieu, A. Omelyanchik and D. Peddis, Structural and Magnetic Properties of $CoFe_2$ O_4 Nanoparticles in an α-Fe_2O_3 Matrix, *J. Phys. Chem. C*, 2025, **129**, 591–599, DOI: 10.1021/acs.jpcc.4c05320.

32 E. Castagnotto, F. Locardi, S. Slimani, D. Peddis, L. Gaggero and M. Ferretti, Characterization of the Caput Mortuum purple hematite pigment and synthesis of a modern analogue, *Dyes Pigm.*, 2021, **185**, 108881, DOI: 10.1016/j.dyepig.2020.108881.

33 P. Maltoni, G. Varvaro, N. Yaacoub, G. Barucca, J. P. Miranda-Murillo, J. Tirabzonlu, S. Laureti, D. Fiorani, R. Mathieu, A. Omelyanchik and D. Peddis, Structural and Magnetic Properties of $CoFe_2$ O_4 Nanoparticles in an α-Fe_2O_3 Matrix, *J. Phys. Chem. C*, 2025, **129**, 591–599, DOI: 10.1021/acs.jpcc.4c05320.

34 A. H. Morrish, *The Physical Principles of Magnetism*, 1965, DOI: 10.1002/9780470546581.

35 F. Bødker, M. F. Hansen, C. B. Koch, K. Lefmann and S. Mørup, Magnetic properties of hematite nanoparticles, *Phys. Rev. B:Condens. Matter Mater. Phys.*, 2000, **61**, 6826–6838, DOI: 10.1103/PhysRevB.61.6826.

36 L. C. Sánchez, J. D. Arboleda, C. Saragovi, R. D. Zysler and C. A. Barrero, Magnetic and structural properties of pure hematite submitted to mechanical milling in air and ethanol, *Phys. B*, 2007, **389**, 145–149, DOI: 10.1016/j.physb.2006.07.042.

37 P. Larese-Casanova and M. M. Scherer, Morin transition suppression in Polycrystalline 57Hematite (α-Fe2O3) exposed to 56Fe(II, *Hyperfine Interact.*, 2007, **174**, 111–119, DOI: 10.1007/s10751-007-9517-4.

38 L. C. Sánchez, J. D. Arboleda, C. Saragovi, R. D. Zysler and C. A. Barrero, Magnetic and structural properties of pure hematite submitted to mechanical milling in air and ethanol, *Phys. B*, 2007, **389**, 145–149, DOI: 10.1016/j.physb.2006.07.042.

39 R. E. Vandenberghe and E. D. Grave, *Mossbauer Spectroscopy Applied to Inorganic Chemistry*, Springer-Verlag, New York, LLC, vol. 3, 1989.

40 G. Muscas, G. Concas, C. Cannas, A. Musinu, A. Ardu, F. Orru, D. Fiorani, S. Laureti, D. Rinaldi, G. Piccaluga and D. Peddis, Magnetic Properties of Small Magnetite Nanocrystals, *J. Phys. Chem. C*, 2013, **114**, 23378–23384, DOI: 10.1021/jp407863s.

41 E. Van San, E. De Grave and R. E. Vandenberghe, Field-induced spin transitions in hematite powders as observed from Mössbauer spectroscopy, *J. Magn. Magn. Mater.*, 2004, **269**, 54–60, DOI: 10.1016/S0304-8853(03)00561-4.

42 F. Bødker and S. Mørup, Size dependence of the properties of hematite nanoparticles, *Europhys. Lett.*, 2000, **52**, 217–223, DOI: 10.1209/epl/i2000-00426-2.

43 G. Muench, S. Arajs and E. Matijevic, The Morin transition in small α-Fe, *Phys. Status Solidi A*, 1985, **92**, 187–192.

44 H. M. Lu and X. K. Meng, Morin temperature and Néel temperature of hematite nanocrystals, *J. Phys. Chem. C*, 2010, **114**, 21291–21295, DOI: 10.1021/jp108703b.

45 J. Wang, V. Aguilar, L. Li, F. Li, W. Wang and G. Zhao, Strong shape-dependence of Morin transition in α-Fe2O3 single-crystalline nanostructures, *Nano Res.*, 2015, **8**, 1906–1916, DOI: 10.1007/s12274-014-0700-z.

46 Ö. Özdemir, D. J. Dunlop and T. S. Berquó, Morin transition in hematite: Size dependence and thermal hysteresis, *Geochem. Geophys. Geosyst.*, 2008, **9**, 2008GC002110, DOI: 10.1029/2008GC002110.

47 R. D. Zysler, C. Arciprete, M. Dimitrijewits and C. Saragovi, Annealing effects on structural and magnetic properties of γ-Fe_2O_3 nanoparticles, *J. Magn. Magn. Mater.*, 2001, **230**, 1907–1909.

48 L. Suber, P. Imperatori, A. Mari, G. Marchegiani, M. V. Mansilla, D. Fiorani, W. R. Plunkett, D. Rinaldi, C. Cannas, G. Ennas and D. Peddis, Thermal hysteresis of Morin transition in hematite particles, *Phys. Chem. Chem. Phys.*, 2010, **12**, 6984–6989, DOI: 10.1039/b925371h.

49 S. H. Gee, Y. K. Hong, J. C. Sur, D. W. Erickson, M. H. Park and F. Jeffers, Spin Orientation of Hematite (a-Fe2O3) Nanoparticles During Morin Transition, *IEEE Trans. Magn.*, 2004, **40**, 2691–2693.

50 R. D. Zysler, M. Vasquez-Mansilla, C. Arciprete, M. Dimitrijewits, D. Rodriguez-Sierra and C. Saragovi, Structure and magnetic properties of thermally treated nanohematite, *J. Magn. Magn. Mater.*, 2001, **224**, 39–48.

51 C. Belviso, M. Mancinelli, M. Abdolrahimi, M. Sturini, F. Cavalcante, A. Lettino and D. Peddis, Red mud treated with KOH: synthesis of sustainable materials from waste for water treatment, *Environ. Sci. Pollut. Res.*, 2024, **31**, 45414–45424, DOI: 10.1007/s11356-024-34083-2.

52 C. Rath, K. K. Sahu, S. D. Kulkarni, S. Anand, S. K. Date, R. P. Das and N. C. Mishra, Microstructure-dependent coercivity in monodispersed hematite particles, *Appl. Phys. Lett.*, 1999, **75**, 4171–4173, DOI: 10.1063/1.125572.

53 H. Qian, G. Han, H. Yang, G. Lin and R. Xu, Investigation on Magnetic Properties of Hematite Superstructures with Controlled Microstructures, (n.d.).

54 V. Baron, J. Gutzmer, H. Rundlöf and R. Tellgren, Neutron powder diffraction study of Mn-bearing hematite, α-Fe2−xMnxO3, in the range, *Solid State Sci.*, 2005, **7**, 753–759, DOI: 10.1016/j.solidstatesciences.2004.11.021.

55 C. Frandsen, C. R. H. Bahl, B. Lebech, K. Lefmann, L. T. Kuhn, L. Keller, N. H. Andersen, M. V. Zimmermann, E. Johnson, S. N. Klausen and S. Mørup, Oriented attachment and exchange coupling of alpha − Fe_2O_3 nanoparticles, *Phys. Rev. B:Condens. Matter Mater. Phys.*, 2005, **72**, 214406.

56 R. Nathans, S. J. Pickart, H. A. Alperin and P. J. Brown, Polarized-Neutron Study of Hematite, *Phys. Rev.*, 1964, **136**, A1641–A1647, DOI: 10.1103/PhysRev.136.A1641.